CFD Applications in Store Separation

H. Özgür DEMİR and B. Tuğcan SELİMHOCAOĞLU
ASELSAN REHİS Business Sector
Konya Yolu 8. Km, Oğulbey Mah. 3051. Sok. No:3
06830 Ankara
TURKEY

hodemir@aselsan.com.tr / tshocaoglu@aselsan.com.tr

Görkem DEMİR
FİGES Engineering
Güzeltepe Mah. Ahmet Rasim
Sok. No:16 06690 Çankaya Ankara
TURKEY

gorkem.demir@figes.com.tr

Prof. Dr. Nafiz ALEMDAROĞLU
Atılım University, School of Civil Aviation
Kızılcasar Mahallesi
Incek Ankara
TURKEY

nafiz.alemdaroglu@atilim.edu.tr

ABSTRACT

This paper presents the results obtained for store separation from various aircraft by CFD methods. Three CFD applications are presented in this paper. The first one presents the computational results, which are validated with the available experimental data of a generic wing-pylon-store configuration (Eglin Test Case) at Mach 0.95. Two different commercially available CFD codes; CFD-FASTRAN an implicit Euler solver and an unsteady panel method solver USAERO, coupled with integral boundary layer solution procedure are used for this application. Major trends of the store separation trajectories are captured with CFD-FASTRAN. Additionally, separation of a fuel tank from an F-16 aircraft wing and full aircraft configurations are solved at Mach 0.3 using the unsteady panel code only. The results and advantages of the two codes for solving the store separation problem are discussed in detail. In the second application, the same Eglin Test Case is investigated where the computational results are obtained using the unstructured Ansys FLUENT. The CFD results obtained for this test case compare very well with the experimental test results. The third study presented in this paper is about standalone separation analysis of a decoy to be dispensed from a fighter aircraft. The decoy used in this study is very similar in geometry to a countermeasure flare used for electronic warfare applications and its trajectory is predicted using a 3DOF flight dynamics code. The aerodynamic coefficients input to the code as well as its validation are performed using Ansys FLUENT. The trajectories of the decoy were obtained for 3DOF/6DOF unsteady CFD and 3DOF quasi-steady flight dynamics analyses with aerodynamic lookup table. It is observed that the CG location, tail size and release Mach number of the decoy play essential roles in the oscillatory motion of the decoy along its trajectory, and therefore its safe separation. It is seen that the statically unstable decoy is able to tumble along its trajectory. Regardless of static stability, its motion always consists of high magnitude oscillations.

1.0 INTRODUCTION

Safe separation of a store from an aircraft is one of the major aerodynamic problems in the design and integration of a new store to an aircraft. Carriage loads and moments acting on the store should be correctly predicted in order to have an idea about its separation behavior. It is difficult to predict correctly the aircraft flow field especially in the transonic regimes since the aerodynamics of the flow field is highly nonlinear and dominated by shocks. The interaction between the store and the pylon affects the attitude of the store after its release. Therefore, time consuming and costly wind-tunnel and flight tests are needed in order to obtain the necessary carriage and trajectory data. Since computational methods for the trajectory calculations give reliable data with less time and cost, they are extensively used before and after the wind tunnel and flight

tests to obtain the optimum integration and separation configurations for the store. This paper brings together the research results of three previous investigations [1,2,3] on store separation and trajectory prediction by CFD techniques. Different CFD techniques and solution procedures are brought together in this paper in order to have an insight to realize the extent and the power of CFD techniques in solving such very complex store separation and trajectory prediction problems.

The first one of these research activities is the one presented by H. O. Demir [1]. The second one is the one presented by G. Demir [2] whereas the third one is the one studied by B. T. Selimhocaoğlu [3].

In the first study, two different wing-pylon-store configurations are studied. The first one of these configurations is the well-known Eglin wing-pylon-finned store test case which is solved with the CFD-FASTRAN solver at 0.95 Mach. The second one is the separation of a fuel tank from an F-16 fighter aircraft's wing-pylon configuration and from full F-16 aircraft configuration, which are solved with the USAERO unsteady panel code.

The second study presented in this paper is again related to the Eglin Test Case but using a different Euler solver, Ansys FLUENT.

The third test study is different from the previous two in terms of the geometry used for the store. It is about standalone separation analysis of a decoy to be dispensed from a fighter aircraft. The store used for this test case is a very small store having dimensions of a standard flare and separation directions are as if it is separated from an F-16 aircraft. This is an interesting problem to analyze since the store tumbles after its ejection in certain circumstances. The trajectory of the store is computed and the results are analyzed in detail and the stability of the trajectory and the tumbling motion of the decoy are discussed.

Therefore, rather than presenting a detailed research topic on a single store separation problem, it is intended in this paper to focus on analyzing the available techniques of CFD methods for computing the flow patterns over the stores and calculate the aerodynamic forces and moments acting on the stores to predict the trajectory of the store following its separation.

1.1 Eglin Test Case Solution by Euler-Overset Method and Unsteady Panel Method for a Fighter Aircraft

Eglin wing-pylon-finned store test case is solved with the CFD-FASTRAN solver at a Mach of 0.95. The well-known Eglin test configuration [4] is given in Figure 1. Store geometry is modeled with the sting, same as used during the experiments. The detailed geometry definitions can be found in References [4] and [5]. There are several reports that successfully predict the trajectory characteristics of this problem [5-7]. The results of the present computations are compared with the available experimental and computational data. It is observed that all of the major trends of the trajectory for this particular problem are captured with the present Euler solution technique.

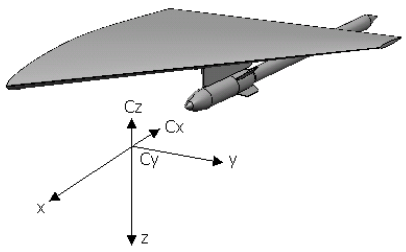

Figure 1: Coordinate Axis System (Eglin Test Case Configuration).

Figure 2: Eglin Configuration without Sting.

The next case solved is the same Eglin Test Case configuration at two different Mach numbers; Mach 0.3 and 0.6. Both CFD-FASTRAN and USAERO are used to find out the carriage loads and moments, which are acting on the store. Base-cut configuration is preferred rather than a smooth revolved store base since in order to have a reasonable drag value, the separated flow must be modeled using a *base wake* in USAERO panel code (Figure 2). Finally, the separation of a fuel tank from an F-16 fighter aircraft's wing-pylon configuration and a full F-16 aircraft configuration are demonstrated with the use of USAERO unsteady panel code (Figure 3).

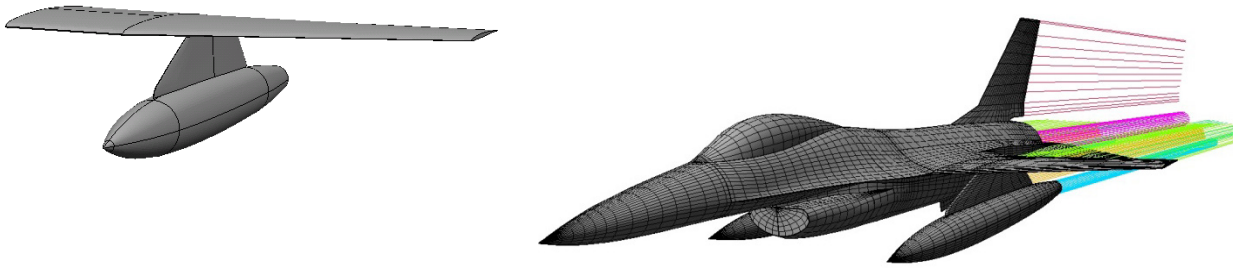

Figure 3: F-16 Wing/Pylon/Fuel tank (left) and Full Aircraft Configuration (right).

The aim of this F-16 aircraft solution with an unsteady panel code is to investigate if there is a large fuselage effect, which contributes to the separation phenomenon. Since there is no experimental data available for this study, the choice of the store weight, ejector forces and application locations may be unrealistic. However, the choice of these parameters is not very significant since the aim of this case study is to investigate the fuselage effect on the store trajectory. The mass of the fuel tank is taken as 250 kg as if it is nearly empty before the separation. Moment of inertia calculation is done by the code USAERO, by assuming that the given mass value is evenly distributed over the entire store. The c.g. location of the fuel tank is chosen at the midpoint location of the longitudinal axis passing from the nose of the store. The ejector forces applied to the store are placed at 15 cm. aft and forward of the c.g. location, with values of 4000 N and 6000 N respectively.

1.2 Eglin Test Case Solution by Ansys FLUENT

The test case in the second study is exactly the same geometry as the one used in the first study, with only difference in the solution method. The commercial CFD code Ansys FLUENT is used for solving the Euler equations. The CFD method used in solving the Euler equations is the moving grid technique instead of the Chimera technique of grid movement as used in the previous study.

First of all, two different standalone store configurations without the wing are used to validate the capabilities of the Ansys FLUENT solver comparing with the available experimental data [8]. The computational results are compared using the non-dimensional pressure coefficient (Cp) distribution from upstream at ϕ=265° angular cut. The results demonstrate that the computational results are compatible with the test data and the Ansys FLUENT solver is a reliable tool to analyze such problems.

The first validation case is a "store alone" configuration with a sting (Figure 4), which is similar to wind tunnel configuration used in Eglin Test Case (Figure 1), while the second validation case is "two stores side-by-side" configuration (Figure 5) to investigate the capability of the Ansys FLUENT solver when there is strong interaction between the two wall boundaries. The distance between the two stores is 1.8 diameters of the store body in the second validation case. The steady state solutions at 26000 ft pressure altitude for a Mach number of 0.95 are obtained to calculate the non-dimensional pressure coefficient distribution on the store. The computational results are obtained by Roe's flux splitting scheme and higher accuracy is achieved by using second order discretization scheme. Approximately 500 iterations are done to obtain the converged

solution and the residuals dropped below 1.0E-08. The computational results are consistent with the experimental data as illustrated in Figure 4 and Figure 5.

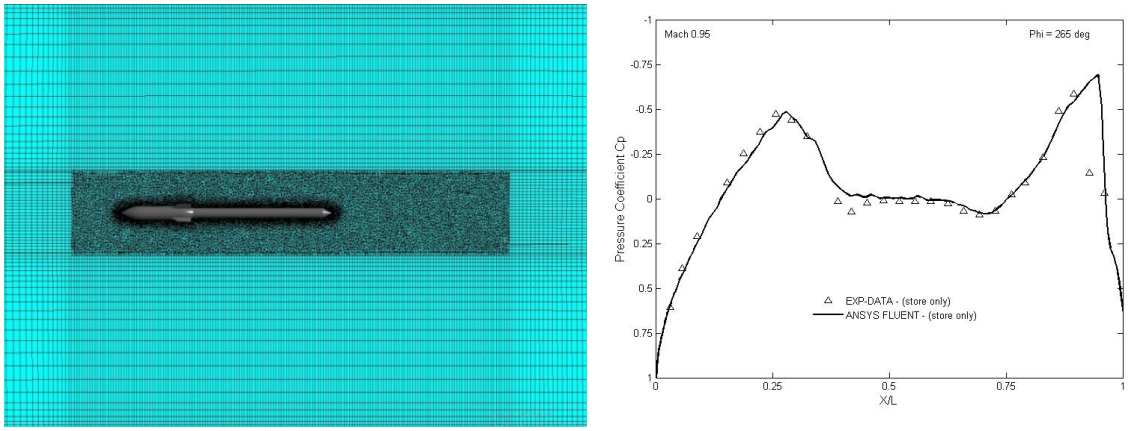

Figure 4: Grid elements around the store (left) and comparison of pressure coefficient distribution on the store with experimental data (right).

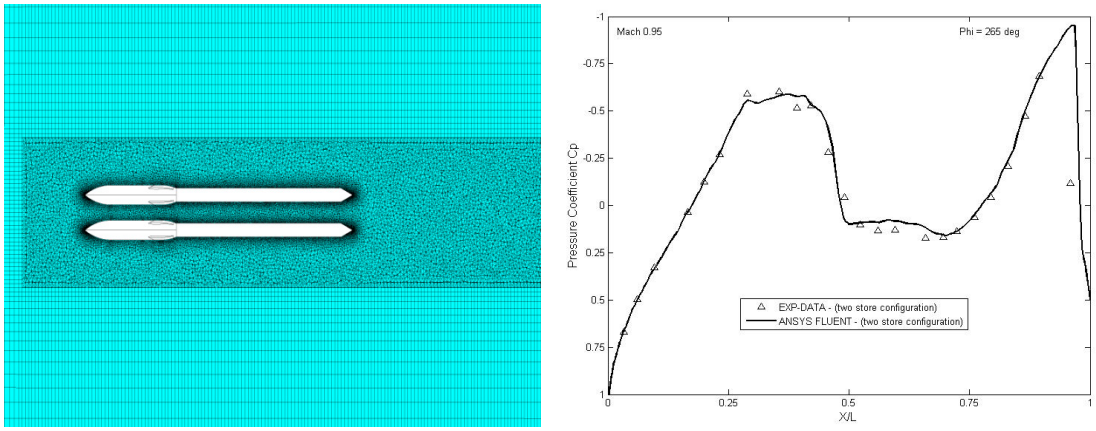

Figure 5: Grid elements around the stores (left) and comparison of pressure coefficient distribution on the store with experimental data (right).

1.3 Decoy Separation

For military aviation purposes, decoys are generally utilized as countermeasures such as flares for protecting against infrared-homing missiles or counter-measures that deploys electronic warfare methods to deceive the radar-guided missiles. Whenever a decoy is released in flight, there are two requirements for the decoy to satisfy: safe separation from the aircraft and its effectiveness, which is the ability to effectively deceive the threat. Safe separation requirement, which is one of the main drivers of decoy aerodynamic design, is investigated in this study (Figure 6).

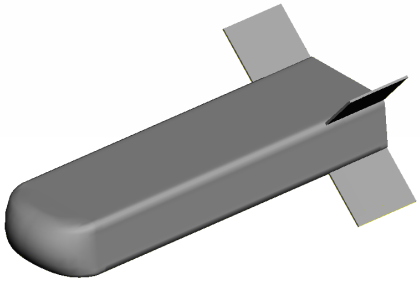

Figure 6: Sample Decoy Geometry.

The decoy aerodynamics team could obtain the huge matrix of data obtained at required safe separation conditions (aerodynamic coefficients of decoy at angle of attack/sideslip, Mach number, aircraft attitude etc.) by means of computational fluid dynamics analyses (CFD), wind tunnel testing or flight testing. As wind tunnel and flight testing techniques are time-consuming and costly, CFD analyses come to the rescue since they are cheaper and more suitable for such iterative design work.

The aerodynamic design team needs a cheap, fast and reliable iterative design tool to obtain the initial configuration estimates (Center of Gravity, Tail Sizing, release Mach number). The methodology used for this purpose in this study consists of numerically integrating the 3-degree-of-freedom (3DOF) flight dynamics equations (longitudinal, vertical, pitching) in a quasi-steady manner. These equations model the aerodynamics of the decoy with the help of tabulated aerodynamic data. The methodology is validated by comparing the results obtained with transient 6-degree-of-freedom CFD results, in terms of trajectory, orientation and attitude time history of the decoy motion.

2.0 METHODOLOGY

2.1 Eglin Test Case by Euler – Overset Grid and Unsteady Panel Method Application

In this study, two separate computational tools are used; which are CFD-FASTRAN, and USAERO. Overset grid technique is very often used for relative body motion problems. CFD-FASTRAN is one of the codes that use implicit Euler/Navier-Stokes flow solver with chimera overlapping grid technique for relative body motion problems. This code is validated for the Eglin Test Case and the results are presented in [9] and a similar technique of solution was further used to validate the simulation of a jettisoned aircraft canopy trajectory [10]. Also, JDAM separation results from an F-18 aircraft are also published in [11]. The wing and the pylon geometries are immersed in an H type grid using multi-block grid technique and the outer boundary of the store domain is set as the overset boundary condition (Figure 7).

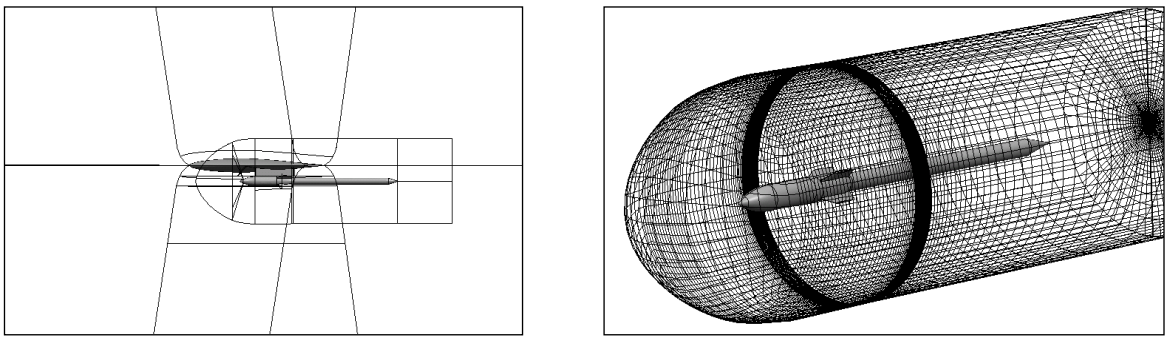

Figure 7: Eglin Test Case Grid Topology with Overlapping Store Grids (left) and Store Computational Domain, Overset Boundaries (right).

USAERO, a time-stepping panel method coupled with a wake model and thin boundary layer assumption with Flight Path Integrator (FPI) module, is the other code used for the present store separation problem. Since the modeling and the solution time of a panel code is considerably less than that of the Euler solutions, panel codes are used as an engineering tool in achieving practical objectives [12]. Same configuration without the sting attachment to the store is solved at Mach numbers of 0.3 and 0.6, with the USAERO code. 2712 body panels are used to model the Eglin configuration (Figure 8) whereas 4117 and 6046 body panels are used to model F-16 wing-pylon-fuel tank and half of the F-16 full aircraft configurations (Figure 9), respectively. For free shear layer simulation, a wake model is also introduced using the other pre-processor, SPIN(w) of USAERO.

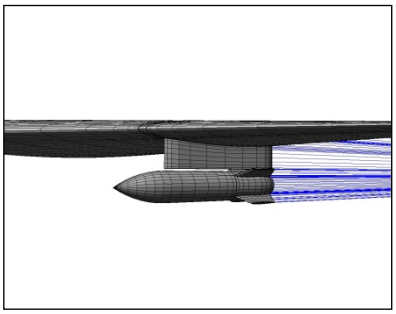

Figure 8: Paneling of Eglin Configuration.

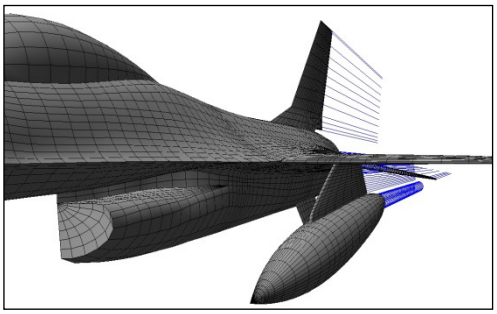

Figure 9: Paneling of F-16 Aircraft with Fuel Tank.

2.2 Eglin Test Case by Euler Method and Moving Grid Technique

2.2.1 Grid Check and Input for the Simulation

The ejector forces are acting on the store for a duration of 0.06 s. Physical parameters such as the mass, inertial moments and the center of gravity etc. of the store are given in Table 1. The mass, inertial moments, location of the application of the ejector forces remain constant.

Table 1: Solution parameters used in the unsteady simulation.

Mass of the store	907 kg
Center of gravity	1.42 m from store nose
Aft ejector location	1.75 m from store nose
Aft ejector force	1.24 m
Forward ejector location	10676 N
Forward ejector force	0.10 m
Ejector store length	42703 N
Roll moment of inertia	27 $kg.m^2$
Pitch moment of inertia	488 $kg.m^2$
Yaw moment of inertia	488 $kg.m^2$
Freestream mach number	0.95
Aircraft angle of attack	0
Pressure Altitude	26000 ft

The computational grid is shown in Figure 10, which contains 3,593,523 tetrahedral and hexahedral cells generated by Ansys Meshing tool for the wing, pylon and the store configuration. The quality of the mesh was checked with the orthogonal quality and the skewness parameters [13-14]. The orthogonal quality for

the grid is determined using the relation between the grid centroid vector to each one of the neighboring grids centroid and the normal vector of the grid centroid to each of these faces. Second quality parameter is the skewness of the grid. The ideal skewness is obtained with cubic hexahedral elements and the tetrahedral elements with equilateral triangle faces.

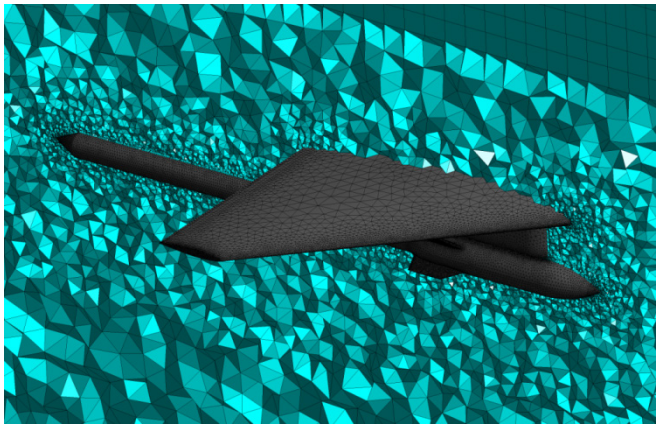

Figure 10: The representation of the computational grid for the Eglin configuration.

The minimum orthogonal quality is about 0.12 for grid elements, and the minimum quality of that computational grid is approximately 0.27 [13-14]. Usually it is acceptable for tetrahedral elements to have a skewness, which does not exceed above 0.85 [13-14]. The maximum skewness of this computational grid is about 0.83.

2.2.2 Flow Solver Ansys FLUENT

The problem is treated as being three dimensional, compressible, and inviscid therefore the flow solver used for the present problem is the Euler's equations given in equations (1-3). The implicit and unstructured mesh solver was used by using the finite volume method [13-14]:

$$\frac{\partial \rho}{\partial t} + \nabla . (\rho \vec{v}) = S_m \tag{1}$$

$$\frac{\partial (\rho \vec{v})}{\partial t} + \nabla . (\rho \vec{v} \vec{v}) = -\nabla p + \rho \vec{g} + \vec{F} \tag{2}$$

$$\frac{\partial (\rho E)}{\partial t} + \nabla . \left(\vec{v} (\rho E + p) \right) = -\nabla . \left(\sum_j h_j J_j \right) + S_h \tag{3}$$

The full multi-grid initialization method [13-14], which can provide a good initial solution with minimum cost of the time spent to accelerate the flow convergence, is used for steady state analysis. The procedure of this method is to simply coalesce groups of mesh elements on the finer grid to form coarser grid elements, then the solution is interpolated to the desirable number of geometric grid levels. This process is repeated until the finest level is reached. In this study, 5 multi-grid levels are used for the full multi-grid initialization. The full multi-grid initialization procedure is shown in Figure 11.

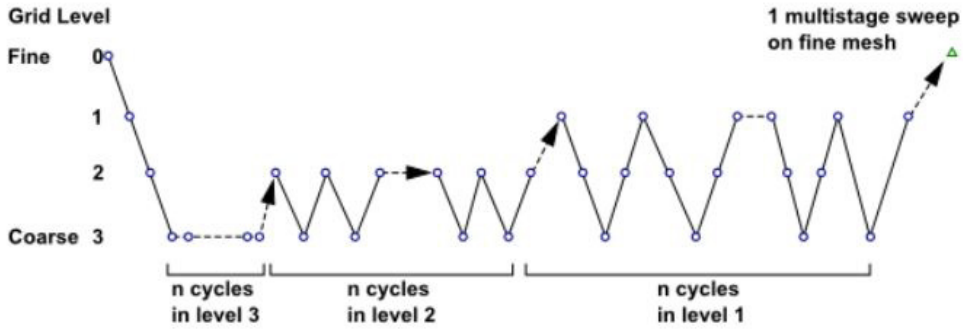

Figure 11: The Full multi grid initialization procedure.

In order to improve the accuracy of the solution, the initial conditions for unsteady analysis are obtained from the steady analysis. Steady analysis approximately converged at 1,000 iterations.

The Convergence criteria was chosen to be as 1E-03, which is generally appropriate for this type of simulations. It is known that the selection of the time step is critical for the convergence of unsteady simulations. It was calculated from equation (4) [13]:

$$\Delta t = \frac{C\Delta x}{U} \tag{4}$$

where C is the Courant number defined by the time scale size, Δx is the typical grid size in the computational domain and U is the characteristic flow velocity in the fluid domain. The maximum Courant number is 50 in transient simulations. The time step was chosen to be as 0.2 ms and 25 sub-iterations are done for each time step. To speed-up the convergence and to avoid the discrepancies of the results generated from initial transient results, 125 sub-iterations are done for the first few time steps.

2.2.3 Trajectory Calculation

The motion of the store during separation is driven by the aerodynamic forces and moments acting on the store center of gravity as well as the gravitational and ejector forces. With Ansys FLUENT, it is possible to utilize the 6DOF solver to compute the trajectory of the store based on these forces and moments. At first, the translational motion of the center of gravity of the store is solved in the inertial coordinate system by using equation (5) [13-14]:

$$\dot{\overrightarrow{V_G}} = \frac{1}{m} \sum \overrightarrow{f_G} \tag{5}$$

where $\dot{\overrightarrow{V_G}}$ is the translational acceleration of the center of gravity, m is the mass of the moving object, $\overrightarrow{f_G}$ is the force vector acting on the store together with the gravity and the ejector forces. The angular motion of the store, $\dot{\overrightarrow{\omega_B}}$, is obtained in the body coordinate system by using equation (6):

$$\dot{\overrightarrow{\omega_B}} = L^{-1} \left(\sum \overrightarrow{M_B} - \overrightarrow{\omega_B} \, x \, L\overrightarrow{\omega_B} \right) \tag{6}$$

where L is the inertia tensor, $\overrightarrow{M_G}$ is the moment vector of the moving object. The moments are transformed from the inertial to the body coordinates by using equation (7):

$$\overrightarrow{M_B} = R\overrightarrow{M_G} \tag{7}$$

where R denotes the transformation matrix given in the equation (8):

$$\begin{bmatrix} C_\psi C_\varphi & C_\psi S_\varphi & -S_\psi \\ S_\theta S_\psi C_\varphi - C_\theta S_\varphi & S_\theta S_\psi S_\varphi + C_\theta C_\varphi & S_\theta C_\psi \\ C_\theta S_\psi C_\varphi + S_\theta S_\varphi & C_\theta S_\psi S_\varphi - S_\theta C_\varphi & C_\theta C_\psi \end{bmatrix} \quad (8)$$

After the angular and translational velocities are computed, they are used in the moving mesh calculations to update the rigid body position.

2.2.4 Moving Grid

The orientation and the position of the computational grids are changed due to the motion of the store caused as a result of aerodynamic forces, moments and additional external effects. The deformation of the mesh elements is controlled by the smoothing method. In this study, the diffusion-based smoothing is used for Euler calculations. The diffusion-based smoothing algorithm is that the mesh motion is governed by the displacement of the boundary of the mesh elements by calculating the mesh displacement velocity using diffusion equation given in equation (9):

$$\nabla(\gamma.\nabla\vec{u}) = 0 \quad (9)$$

where γ is the diffusion coefficient and u is the mesh displacement velocity.

The diffusion coefficient is used to adjust the diffusivity for the penetration of the boundary motion into the surrounding of the interior of the deforming mesh. There are two different diffusion coefficients implemented either in the form of the function of the boundary distance or in the cell volume. The boundary distance formulation (10) was used to calculate the diffusion coefficient. The diffusion coefficient can be manipulated by changing the diffusion parameter. The diffusion parameter is specified as 1.5 to let the "far field" mesh to absorb the motion of the store, such that the grids close to the moving boundary are better preserved:

$$\gamma = \frac{1}{d^\alpha} \quad (10)$$

where d is the normalized boundary distance and α is the diffusion parameter.

The vector equation is discretized using Ansys FLUENT's standard finite volume method, and the resulting matrix is solved iteratively using the algebraic multi-grid solver. The cell centered solution for the displacement velocity u is interpolated onto the nodes using inverse distance weighted averaging, and the node positions are updating according to equation (11):

$$\bar{x}_{new} = \bar{x}_{old} + \bar{u}\Delta t \quad (11)$$

In addition, new cells are generated with re-meshing method if the deformed cells exceed the specified mesh quality and size parameters (maximum skewness, minimum, maximum size limits).

2.3 Decoy Separation

2.3.1 Theory and Numerical Implementation

During most of the flight, the aircraft is going to be in a trimmed level flight condition. If the decoy were to be released during such a flight condition, i.e. in a longitudinal plane, as long as there are no lateral perturbations in the flow around the longitudinally symmetric decoy, **ideally** the decoy should have no

motion in the lateral directions. Hence, the decoy should move strictly in the longitudinal direction eliminating the two rotational and one translational degree-of-freedoms, resulting in a three-degrees-of-freedom motion. The flowfield around the decoy is going to have lateral perturbations and the aircraft is going to be oscillating around both the longitudinal and rotational directions during flight.

2.3.2 Equations of Motion / Coordinate Systems / Aerodynamic Forces and Moments

Equations of motion are written in inertial horizontal, vertical and pitching axes. The decoy studied in this study has **a tail geometry with no control capability and propulsion**, hence the only forces and moment acting on the decoy are the aerodynamic forces and moment written in wind axes. These aerodynamic forces and moment are transformed to inertial axes as well. The aerodynamic forces (drag, lift) are dependent on Reynolds and Mach numbers, while the pitching moment is also dependent on the pitch damping derivative. [14], [15].

2.3.3 Numerical Implementation (3FL-DYN)

The numerical implementation of the problem was done by using four modules: atmospheric conditions module, geometrical properties module, aerodynamic data table lookup module and the time integration module. The flowchart of the numerical implementation is given in Figure 12.

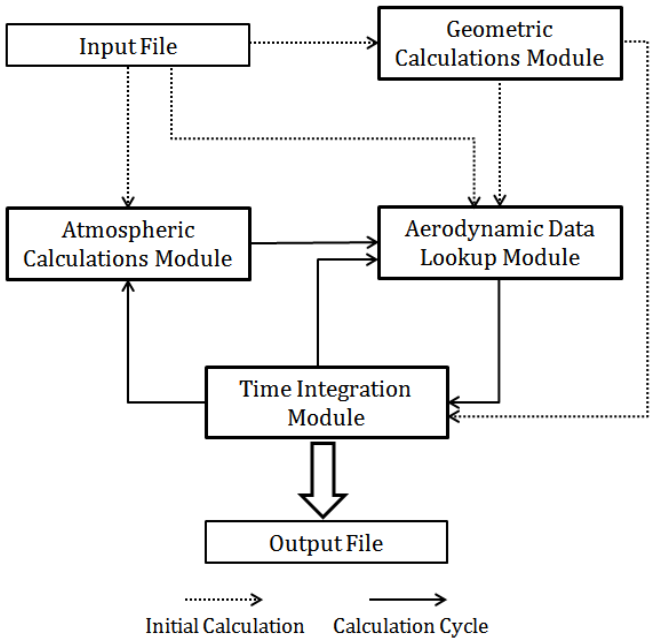

Figure 12: 3FL-DYN FlowChart.

Atmospheric conditions module calculates the ISA conditions [15] at which altitude the decoy is after its release.

Geometric properties module calculates the inertia (only due to CG config., no change with time) and keeps the mass and the tail size information of the decoy.

Aerodynamic data table lookup module reads the decoy aerodynamic data at different Mach numbers and angles of attack and linearly interpolates these data according to the flight parameters of the decoy calculated by the time integration module.

Time-integration module integrates the 3DOF flight equations over time to find the orientation and the position of the decoy after one time step utilizing Runge-Kutta time integration algorithm [16].

2.3.4 Calculation of Aerodynamic Coefficients

In this section, two different methodologies for calculating the aerodynamic coefficients of the decoy are compared with each other. One of the methodologies is a lower order method based on empirical data (DatCOM) while the other is based on the numerical solution of the decoy flow field. (CFD, Fluent).

To obtain the aerodynamic coefficients with FLUENT, steady, compressible analyses at different Mach numbers, angles of attack and tail sizes are performed. For the pitch damping derivative, however, transient analyses in which the decoy is rotating around the pitching axis at constant angular speed are performed. 1st order time discretization and 2nd order spatial discretization with realizable k-epsilon turbulence model are utilized [17], [18].

For the grid independency of CFD solutions, surface meshes with 4 different sizes are created with HyperMesh pre-processor software [19] and steady CFD solutions at five angles of attack (three of which are very high) are performed. The finest grid, whose properties are given in Table 2, is taken as reference. According to these results, Grid 3 (Figure 13) was used for all the steady and transient CFD analyses carried out throughout the study. Due to the fact that Grid 3 has 23.7% less number of elements compared to Grid 4 and a maximum error of 3.5% occurring at very high angles of attack, it is considered to be an optimized solution with acceptable accuracy and cost, especially for the 6DOF transient CFD analyses explained in following sections.

Table 2: Surface Grid Properties and the Relative Error Values.

Grid #	Surface Grid Size	Total Grid Size	Largest Relative Error (%)		
			Drag	Lift	Moment
1	32856	1126275	8.8	8.9	51.3
2	71434	1744834	4.5	5.9	37.8
3	104986	2798373	2.9	0.8	3.5
4	141498	3667583	–	–	–

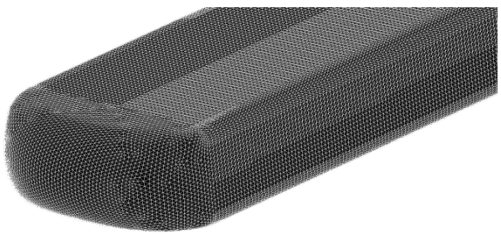

Figure 13: Decoy Surface Grid (Grid 3).

Figure 14 clearly shows that the results of two methodologies are not similar. Generally, DatCOM predicts smaller forces and moments. The differences between two methodologies are especially greater for lift and moment coefficients. For M = 0.6, the lift coefficient predicted by FLUENT is two and a half times the value predicted by DatCOM at 50° angle of attack. Besides, in some cases the trends of the results are not similar either. Based on such differences observed, FLUENT solutions were decided to be the reference solutions because of higher level of equations solved with compressibility and separated boundary layer effects.

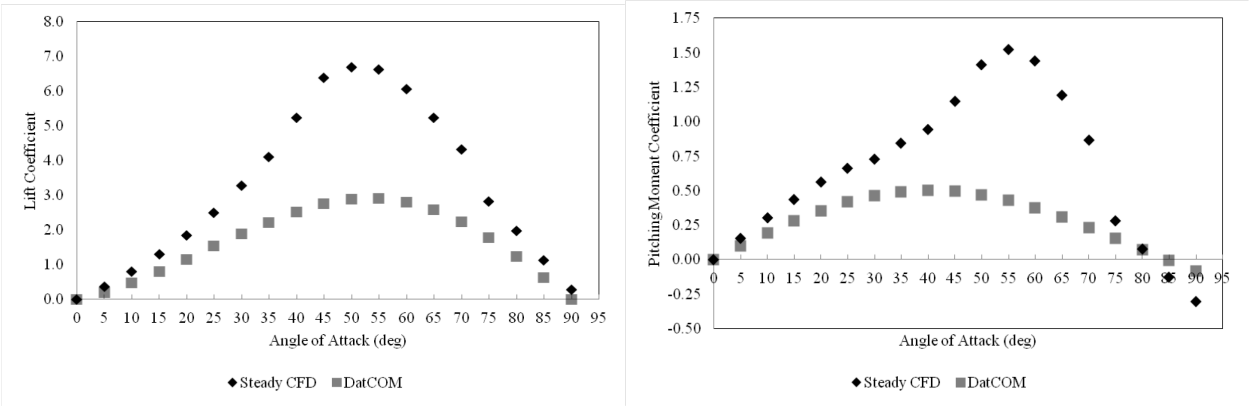

Figure 14: Comparison of DatCOM – CFD Methodologies at M = 0.6 for Lift (Left) and Pitching Moment (Right) Coefficients.

2.3.5 Assessment of the Methodology

In this section, time step selection for 3FL-DYN and transient CFD analyses as well as the necessity of pitch damping derivative and the evaluation of 3DOF assumption subsections are given. From this point on, time histories of Euler Angles and angular rates / accelerations as well as trajectories are going to be given as results. These quantities are non-dimensionalized with a reference value and given with the subscript of "nd". Time is non-dimensionalized with respect to flight duration, while decoy geometry is non-dimensionalized with respect to the reference length. The decoy is released nearly perpendicular to the flow (AoA ≈ 90°).

2.3.5.1 Time Step Selection

Both the 3FL-DYN and the transient CFD analyses are based on the integration of certain variables like acceleration or velocity with time. The time step utilized in the integrations directly affects the accuracy of the integrated quantities, but a very small time step is going to increase the calculation cost in terms of time and computational power. Hence, a time step yielding sufficient accuracy with an optimization of calculation cost should be selected.

Time Step Selection for 3FL-DYN

For the evaluation of the time step size for 3FL-DYN, pitch angle and pitching rate vs. time graphs are plotted for different time step sizes for a dynamically stable case at two different Mach numbers. The results obtained with smallest time step are taken as reference and to reduce the computational cost with acceptable accuracy, a time step of 0.02 ms is selected for the dynamic analyses with 3FL-DYN (Figure 15).

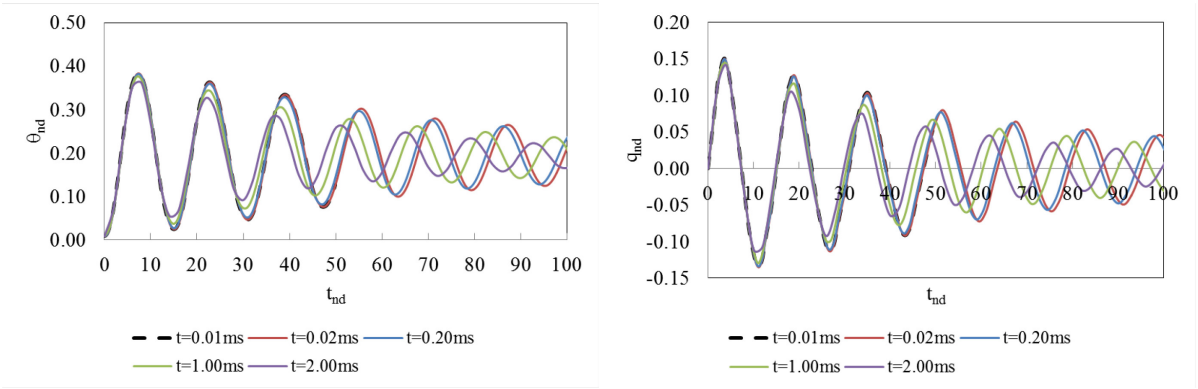

Figure 15: Time Step Selection for the 3FL-DYN Code (Left: Pitch Angle / Right: Pitching Rate).

Time Step Selection for Transient CFD Analyses

To select the time step size for transient CFD analyses, solutions utilizing 6DOF motion were carried out at a statically unstable M = 0.6 case to evaluate the solution on the lateral direction in more detail. If the decoy does not have static stability, the lateral motion is going to be easier to observe. Static stability is evaluated with the 3FL-DYN code. Due to the 3DOF nature of 3FL-DYN, the main Euler angle used for comparison in this study is the pitch angle. The reference solution is the one with the smallest time step.

Based on the results given in Table 3, a time interval of 0.05 ms was selected for all the transient CFD analyses carried out. Taking the pitch angle into account, a difference of 0.7% was considered to be sufficient. Although there is a difference of 5.4% for the roll angle (ϕ), the transient CFD solution duration of 0.02 ms is roughly 2.5 times the 0.05 ms time interval, which takes about 3-4 weeks for converged solution time with a standard workstation for transient 6DOF solutions. Hence, an optimized trade off was made between calculation cost and solution accuracy in the lateral directions with the selection of a 0.05 ms time interval.

Table 3: Maximum Relative Errors for Different Time Steps Used in Transient CFD Calculations.

	Maximum Relative Error (%)		
Time Step	Roll Angle	Pitch Angle	Yaw Angle
0.02 ms	–	–	–
0.05 ms	5.4	0.7	2.8
0.20 ms	9.6	5.0	11.7
0.50 ms	27.7	4.1	16.5

2.3.5.2 Pitch Damping Term Requirement in 3FL-DYN

In this study, initially the pitch damping term was not included in 3FL-DYN. However, the resulting model turned out to have insufficient and unphysical damping characteristics (behaving as a stiff spring) making it nearly impossible to find a configuration working effectively as a countermeasure against threats.

In order to obtain the pitch damping terms at different angles of attack and Mach numbers, transient CFD methodology is utilized. The additional moment coefficients are obtained by the difference of analyses at a pitching rate of zero (steady) and transient analyses. [20]

The time variation of pitch angle and pitching rate results confirm the necessity of the addition of pitch damping term (Figure 16). When the results are compared, the rate of decrease in magnitude of the oscillations indicate that, the model with pitch damping derivative is superior due to the fact that the oscillations observed in all figures demonstrated a decrease in increasing rate. Moreover, taking the results given in the following chapters into account, the case with the pitch damping derivative was found out to be closer to the transient CFD results.

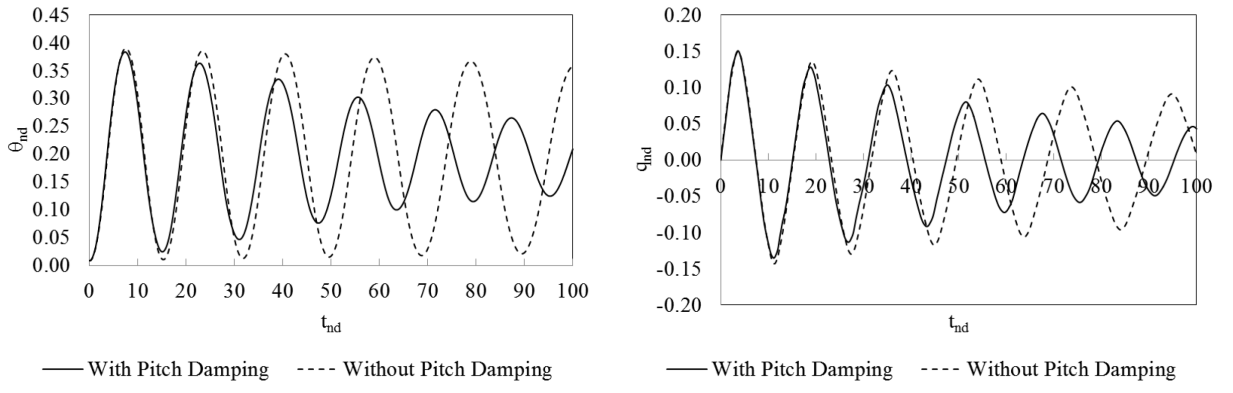

Figure 16: The Effect of Pitch Damping Term at M=0.6 (Left: Pitch Angle / Right: Pitching Rate).

2.3.5.3 Evaluation of 3DOF Assumption

When the equations of motion in 3DOF are written, the lateral forces, moments and aerodynamic derivatives are not included. Hence, due to neglected lateral terms in 3DOF motion, even if the decoy is showing favorable behavior, it may not be the case for 6DOF motion. To evaluate the 3DOF assumption, the CFD solution of two different cases, one of which is 3DOF and the other 6DOF, is compared in terms of trajectory, angle, velocity, acceleration, forces and moments. The CFD solutions are performed with "dynamic meshing" and "UDF" (User-Defined-Function) features of FLUENT. [13, 14]

The analyses were performed for two different center of gravity values, CG1 and CG2 at two different Mach numbers of 0.3 and 0.6. At CG1 location, the decoy does not have static stability, whereas at CG2 location, the decoy is statically stable. Looking at the results given in Figure 17, at CG2, it is clear that the 3DOF CFD and 6DOF CFD results are similar in trend. As there are neglected stiffness and damping terms in 3DOF solutions, the oscillation magnitude decreases slower compared to 6DOF solutions. Taking the initial design purpose of 3DOF approach into account, the assumption is considered to be sufficient. CG1 location results are not consistent at all. It is understood that in order for the 3DOF assumption to work effectively, the cases investigated should have static stability. In the absence of static stability, the motion in the lateral direction is dominant proving the assumption of 3DOF to be invalid.

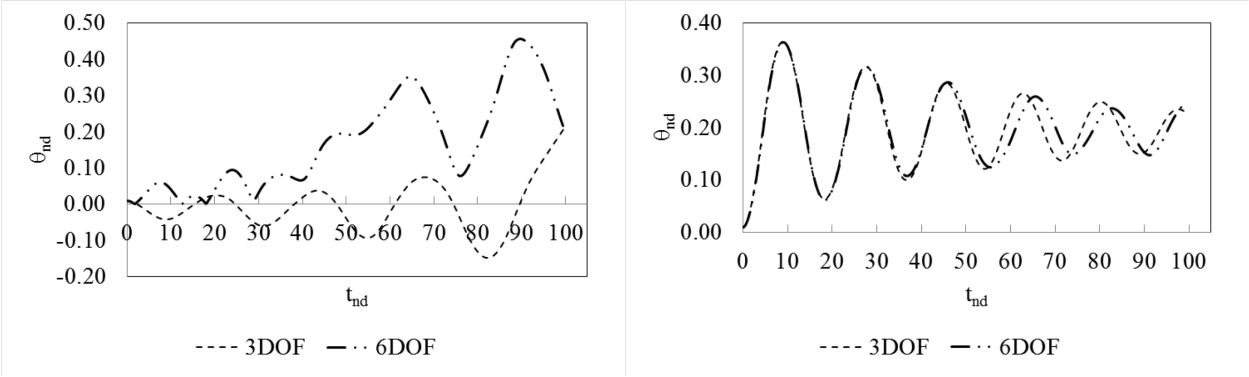

Figure 17: Comparison of 3DOF and 6DOF transient CFD analyses at Mach 0.6 (Left: CG1 / Right: CG2).

At Figure 18, for CG2 location, a continuous rolling motion as well as an oscillating yawing motion with magnitudes smaller than that of the pitching motion is observed. Patel, Sowle et al. [21] state that according to the wind tunnel results even if the angle of sideslip is zero, due to asymmetrical vortex shedding, at high angles of attack large side forces and dynamic out-of-plane loadings may occur, resulting in a yawing motion. As high angles of attacks occur during the pitching motion, a continuous rolling motion is inevitable with coupling of the yawing and pitching motion and one order smaller mass moment of inertia in the roll axis. In addition, the effect of rolling motion of the statically stable decoy is similar to that of a roll-stable missile, which utilizes the conservation of angular momentum for lateral stability during flight. [22]

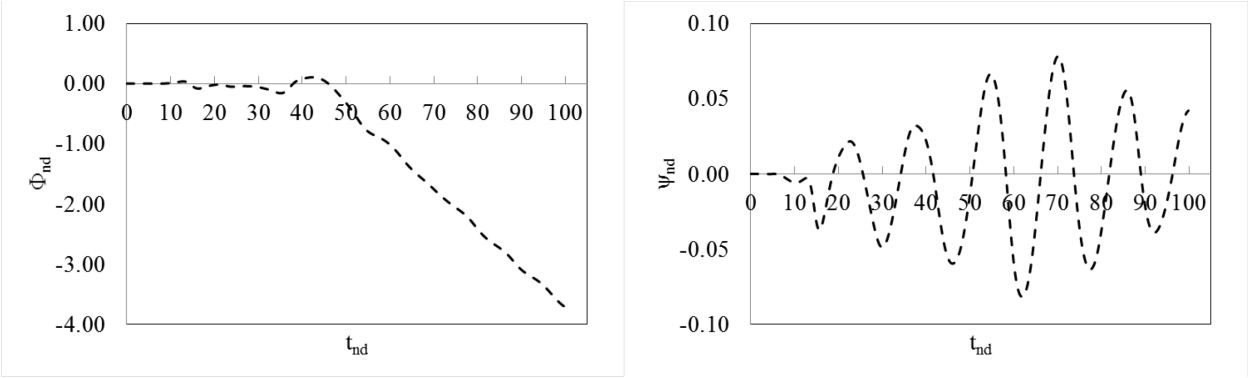

Figure 18: Time Variation of Roll (Top) and Yaw (Bottom) Angles obtained from transient 6DOF CFD analyses at CG2 location.

3.0 RESULTS AND DISCUSSION

3.1 Eglin Test Case Euler Solution with Overset Grids

Eglin test case is solved using CFD-FASTRAN with overlapping grid methodology. The results given below represent the linear and angular displacements as well as the velocities and pressure distributions on the store at four different angular positions and the time history of the force coefficients. It is observed that all of the major trends are captured when one compares the results with those given in [5].

Store moves towards inboard and backwards while moving down with the effect of gravity and the ejector forces after its release. Total forces acting on the store result in a pitch up, yaw and roll to the outboard motion (Figure 19). Aerodynamic forces acting on the store result in a pitch down moment [5], which can be seen after the vanishing of the ejector forces effects. The effect of the ejector forces can be clearly seen from

Figure 20. The angular pitch rate starts to decrease after t=0.05 s, corresponding to the end of the stroke. The discrepancy between the velocity data and the results obtained increases after t=0.2 seconds due to the differences in angular orientations [5]. This difference also affects the force coefficients history as seen in Figure 22. Although there are small discrepancies between the present results and the experimental data, it is observed that the general trends for all the curves are captured.

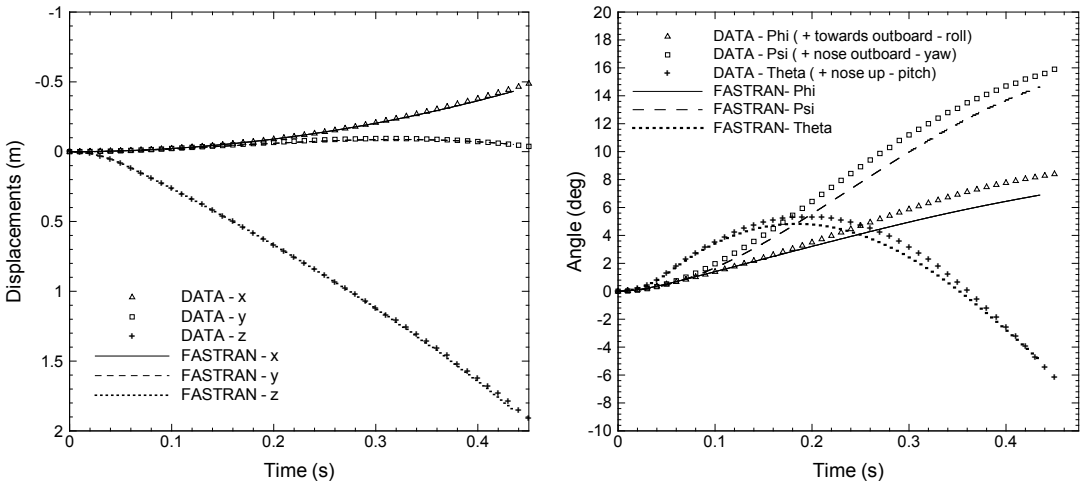

Figure 19: Linear and Angular Displacements, Eglin Validation Test Case, M=0.95.

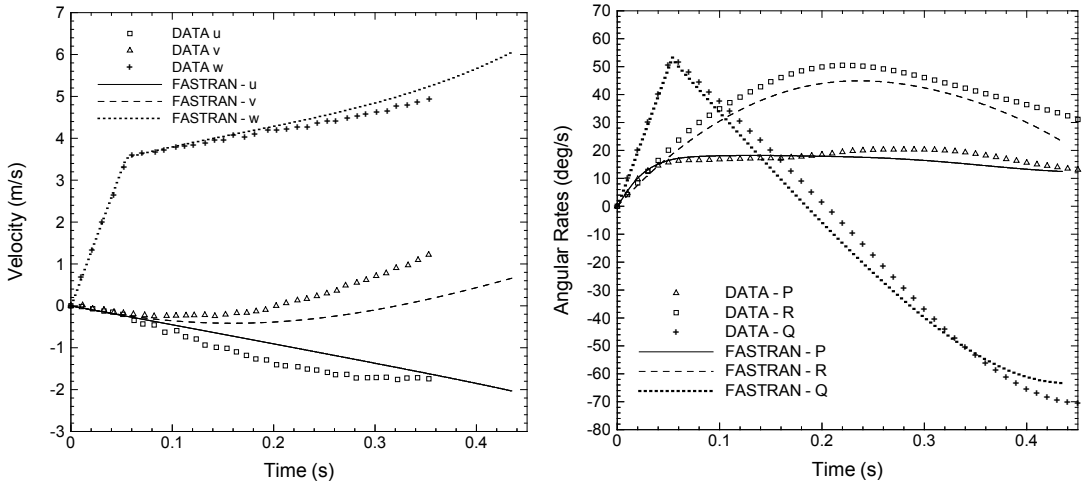

Figure 20: Linear and Angular Velocities, Eglin Validation Test Case, M=0.95

Figure 21 shows the pressure coefficient distribution on the store at the captive carriage position (t=0). Interaction effects between the store and the pylon can be seen from these graphs. ϕ=5° cut plane location is in the gap region between the pylon and the store. The compression due to pylon and the expansion after the compression is well captured. Outboard yawing moment tendency of the store can be predicted from the pressure coefficient distribution graphs at $\phi=95^0$ and $=275^0$ locations. Shock locations are also well predicted.

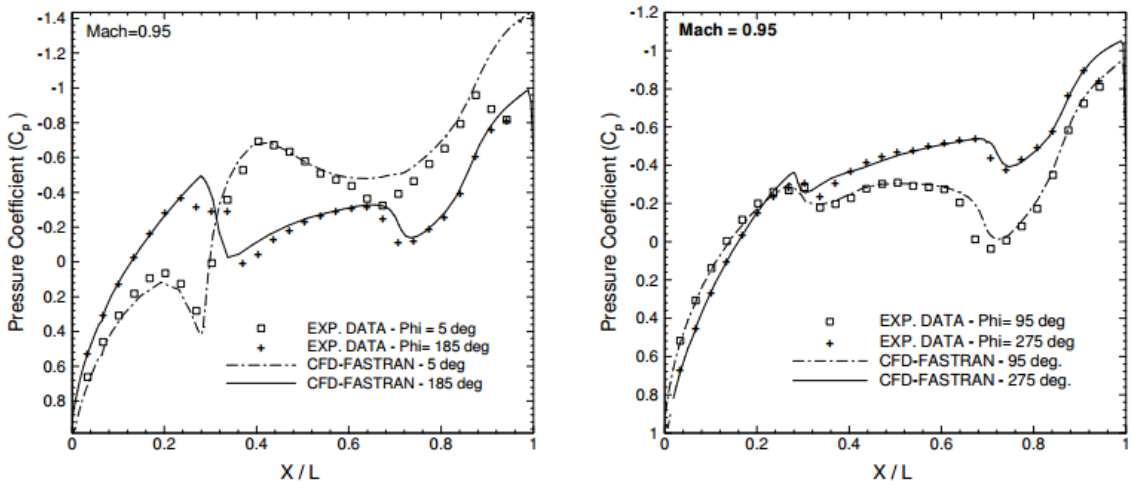

Figure 21: Pressure Distributions on the Store in Captive Position, Eglin Validation Test Case, M=0.95.

Time histories of the force coefficients graph are given in Figure 22. C_x graphs are drawn with and without the base pressure correction. The displacements are obtained with the base pressure correction applied to the store. Otherwise, the drag on the store would be higher than the experimental values causing much larger backward displacement.

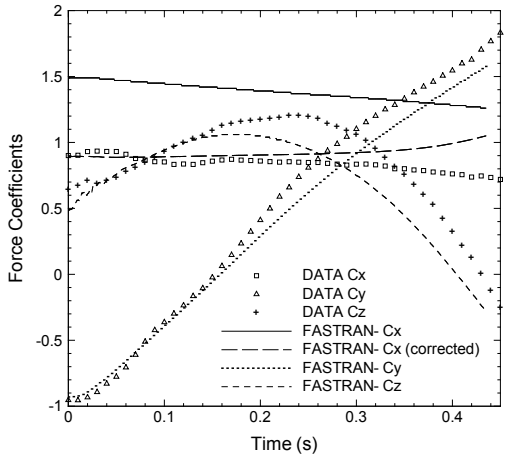

Figure 22: Time History of Force Coefficients on the Store, Eglin Validation Test Case, M=0.95.

No doubt that error is introduced to the results since the solution is obtained without the effects of viscosity. Ejector force approximation could also affect the Euler angles and rates since the correct ejector modeling used in the experiment is not exactly known. Also, the time accurate modeling of the flow would result in a different flow field calculation than the quasi-steady modeling of the experimental results [5]. Despite all these errors, it can be concluded that the CFD-FASTRAN solver can be used in the store separation problems.

Euler vs. Panel Code Solutions using Eglin Test Geometry at M= 0.3 and M=0.6

The same configuration (without sting attached) is solved with both Euler and unsteady panel code at Mach 0.3 and Mach 0.6. The aim is to compare the two methods of prediction tools and the results are given as forces and moment acting on the store and the pressure distribution on the store in its captive position (t=0 s).

Pressure distributions on the store in its captive position are drawn at φ= 0^0, 90^0, 180^0 and 270^0 angle planes and given in Figure 23 and Figure 24. A summary of the force and moment coefficients at captive carriage state are also given in Table 4. The pressure distributions calculated with both codes have the same trend. Interaction between the pylon and the store can be observed in Euler solution at φ=0^0, which is the location between the store and the pylon. The same compression is also observed in the panel method but with a much weaker strength.

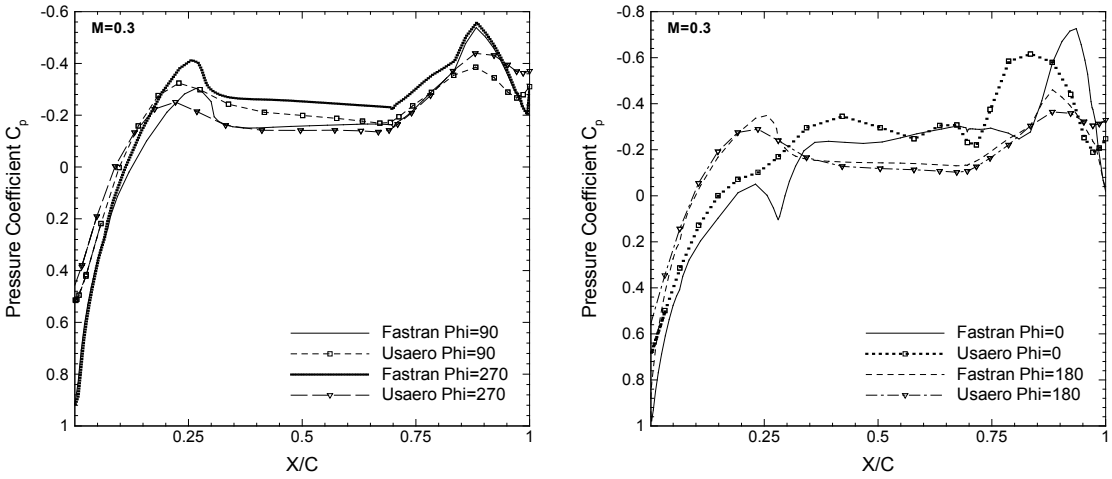

Figure 23: Pressure Distribution on the Store in Captive Position, USAERO and CFD-FASTRAN Results, M=0.3.

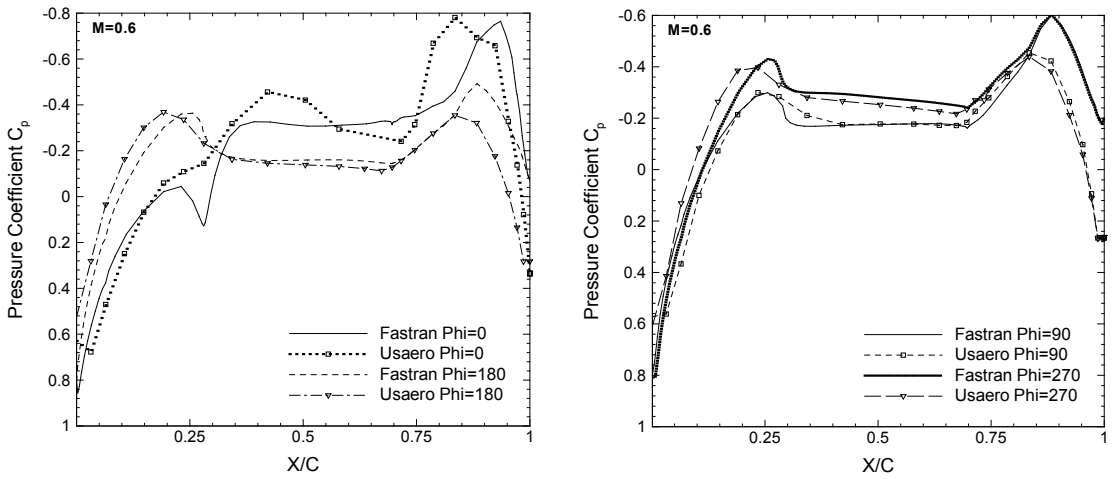

Figure 24: Pressure Distribution on the Store in Captive Position, USAERO and CFD-FASTRAN Results, M=0.6.

Table 4: Force and Moment Coefficients Summary, M=0.3, M=0.6.

Eglin Test Case		CFx	CFy	CFz	CMx	CMy	CMz
M=0.3	FASTRAN	0.384	-0.449	0.695	0.0967	1.702	0.1261
	USAERO	0.128	-0.285	0.695	0.0110	1.465	0.0225
M=0.6	FASTRAN	0.319	-0.507	0.758	0.0938	1.839	0.1111
	USAERO	0.137	-0.362	0.912	0.0130	1.882	0.0406

For $\varphi=90^0$, 180^0 and 270^0 angles, CFD-FASTRAN calculates lower Cp values than the panel code after x/c = 0.75. Same behavior is observed when the Cp distributions are compared with the experimental results in the Eglin case at M=0.95. This difference can be attributed to the nature of the Euler solver, which excludes the effects of viscosity. Boundary layer coupling option when introduced to the panel method improves the Cp distributions obtained by the USAERO code. This difference in pressure distribution results in lower force and moment coefficients values than obtained in CFD-FASTRAN.

3.2 Eglin Test Case Using Euler Solution with Moving Grids

The time dependent analysis of the wing-pylon-finned store configuration is performed using the CFD code Ansys FLUENT with moving grid methodology. The pressure coefficient of steady state solution is compared with the experimental results at ϕ = 5°, 95°, 185° and 275° in Figure 25.

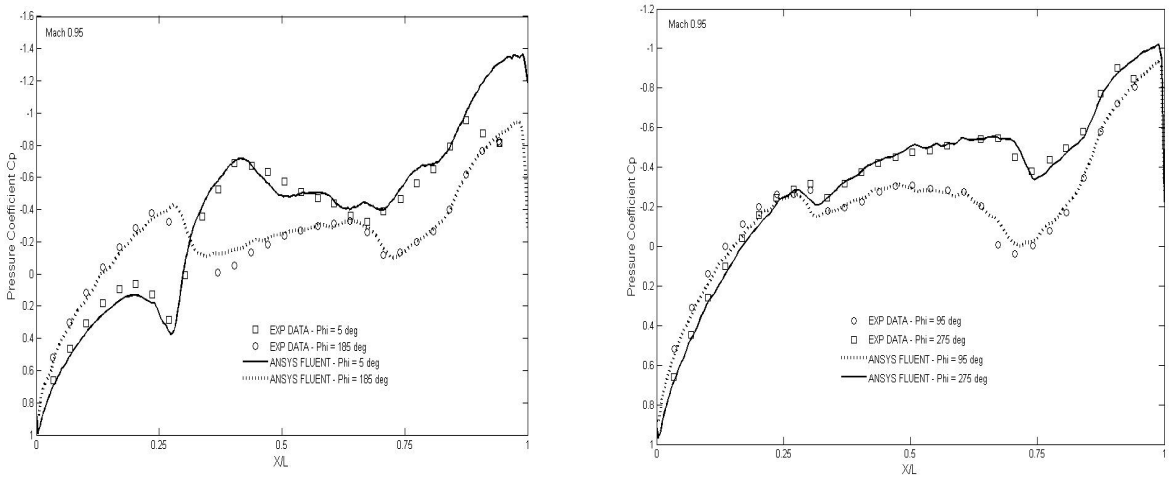

(a) Φ = 5°, 185° **(b) Φ = 95°, 275°**

Figure 25: Comparison of the pressure coefficient with experimental data.

The linear position and angular orientation, linear and angular velocities are compared with the available experimental data in Figure 26 and Figure 27. Linear and angular displacements graphs are given with respect to the store center of gravity location at the carriage. The required memory and CPU times for performing the analyses are given in Table 5.

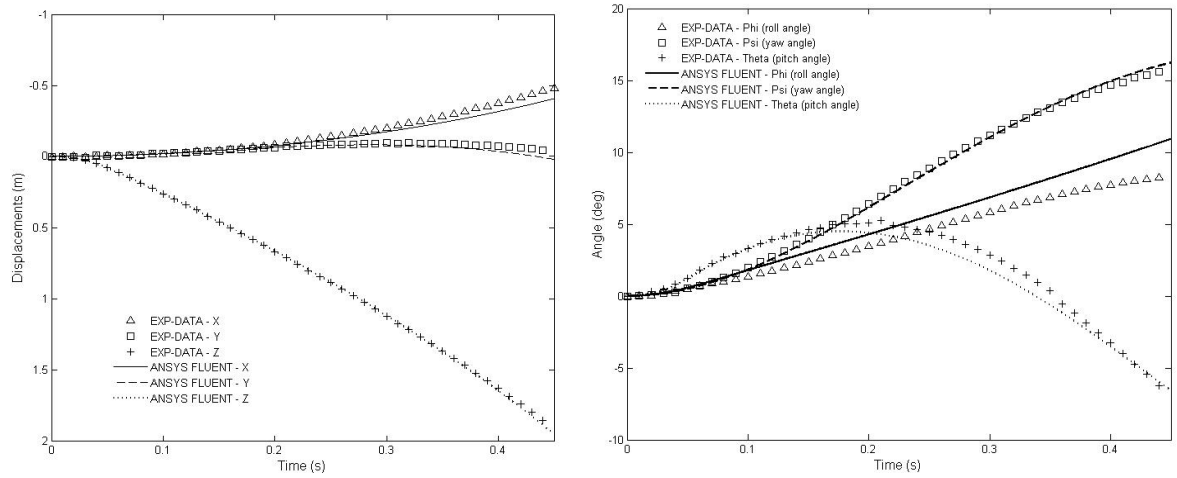

Figure 26: Comparison of linear (left) and angular (right) displacements of the store.

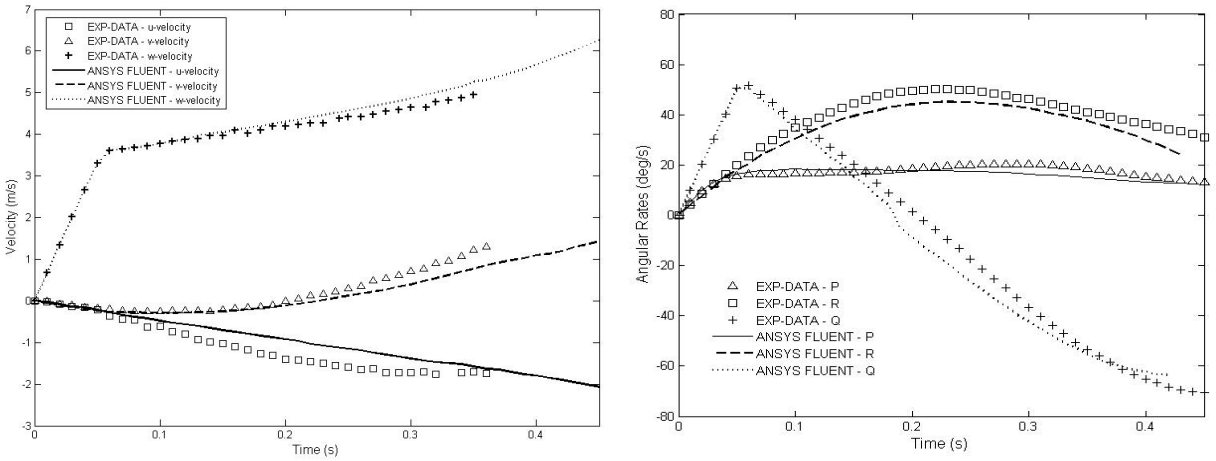

Figure 27: Linear and Angular Velocities of the Store.

Table 5: Required memory and CPU time for simulations.

Solver	Solution Type	Number of Processors	CPU Time	Required Memory
ANSYS FLUENT	Steady State	14	3.3 hrs	1.1 GB
ANSYS FLUENT	Transient	14	96 hrs	142 GB

It is apparent that the displacement in z direction is in very good agreement with the experimental data because the ejector forces and gravity are more dominant than the aerodynamic forces in this direction. The displacements in x and y directions match very well with the experimental data. However, there is some discrepancy in x-direction due to the absence of viscous effects.

The store pitches nose up due to the ejector forces acting on the store until 0.06 s. The store starts pitching down after freed from the ejector forces. Store starts pitching down movement after 0.18 s. The maximum angular difference is 5.04 degrees, which occurs at t = 0.22 seconds.

The store rolls continuously outboard throughout the separation process. The trend of the curve is almost the same with the experimental data. The curve tends to diverge from the experimental data at 0.083 s. The maximum angular discrepancy is 2.69 degrees, which occurs at 0.45 seconds.

The store yaws continuously towards outboard of the wing. The trend of the curve is same with the experimental data. The maximum angular difference is 0.38 degrees, which occurs at 0.41 s.

Linear and angular velocities of the store are given in Figure 27. The linear velocity in downward direction is increasing with almost constant acceleration of 60.17 m/s^2 until the time 0.06 s. After the effect of the ejector forces vanishes, store decelerates. The maximum discrepancy is 0.31 m/s, which occurs at 0.35 s. The linear velocity in side direction does not match very well with the experimental data. The maximum difference between computational results and experimental data is 0.45 m/s at 0.35 s. The linear velocity in backward direction is almost linearly increasing in the flow direction. The trend of the angular velocities is in very good agreement with experimental data. There are some discrepancies due to neglection of the viscous effects.

3.3 F-16 Fighter Aircraft Wing Alone / Full Configuration Cases Using Panel Code

These cases are solved with the panel code only. The aim is to find out the effect of fuselage on the trajectory of the store during separation. The results are given in linear and angular displacements of the store in its trajectory and the pressure distribution on the store in its captive position (t=0 s) right before the separation and the histories of the force coefficients.

Linear displacement graphs are given in Figure 28. Z displacements for both configurations are almost the same. X displacement for the wing alone configuration has the same trend with the full aircraft configuration, but the drag value is higher (Table 6). Therefore, the store separated from the wing moves faster backwards when compared with the full aircraft configuration. The most important difference is observed in the Y displacement. The side force calculated on the store in the wing only case is very small when compared with the force obtained for the full aircraft configuration. As a consequence of this side force, an inboard movement of the store is observed in the full aircraft configuration whereas the opposite is true for the wing alone case.

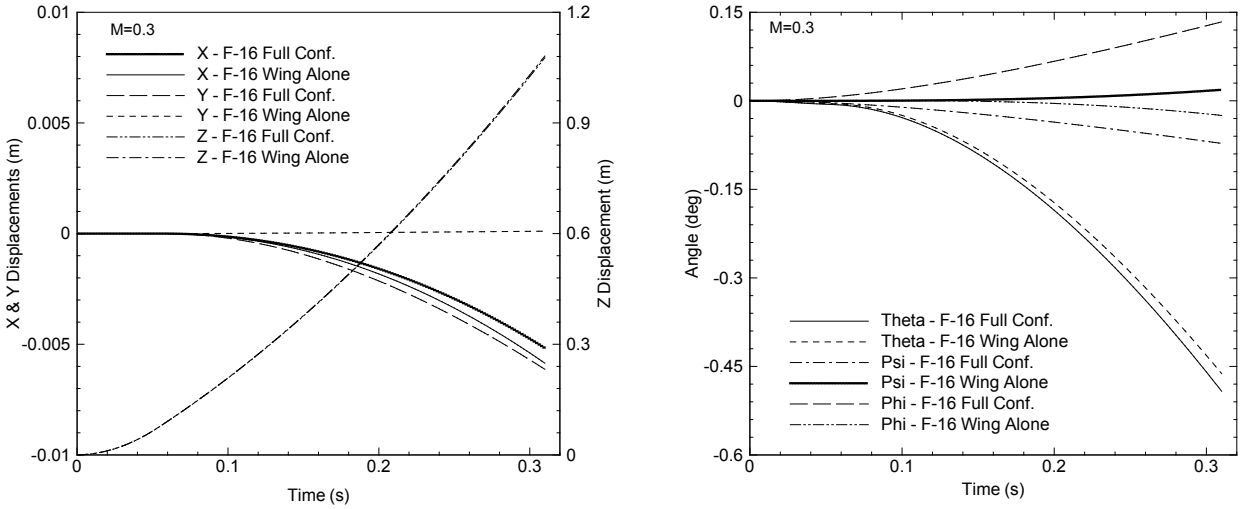

Figure 28: Linear and Angular Displacements, Fuel Tank, M=0.3.

Table 6: Force and Moment Coefficient Summary, M=0.3.

Fuel Tank M=0.3	Wing Conf.	Full Conf.
CFx	0.0506	0.0427
CFy	0.0044	-0.0823
CFz	0.0314	0.0664
CMx	0.0004	0.0034
CMy	-0.7359	-0.7585
CMz	-0.0021	-0.0517

Angular displacement graphs are given in Figure 28. Pitch angle has the same trend for both cases. However, yaw and roll angles have shown opposite behavior. The store separated from the full aircraft configuration rolls outboard and yaws to inboard whereas the store separated from the wing exhibits opposite angular motions.

Pressure distribution graphs are given in Figure 29. Compression due to the pylon is observed with both configurations at $\varphi=0^0$ angle plane. Pressure distributions at $\varphi= 90^0$, and 270^0 plane cuts are almost same for wing configuration and it is observed that there is no significant movement of the store in that direction after separation. However, the pressure on the inboard side of the store is lower than that on the outboard side for the full aircraft configuration. Therefore, the store has a movement towards inboard of the wing when separated from the aircraft.

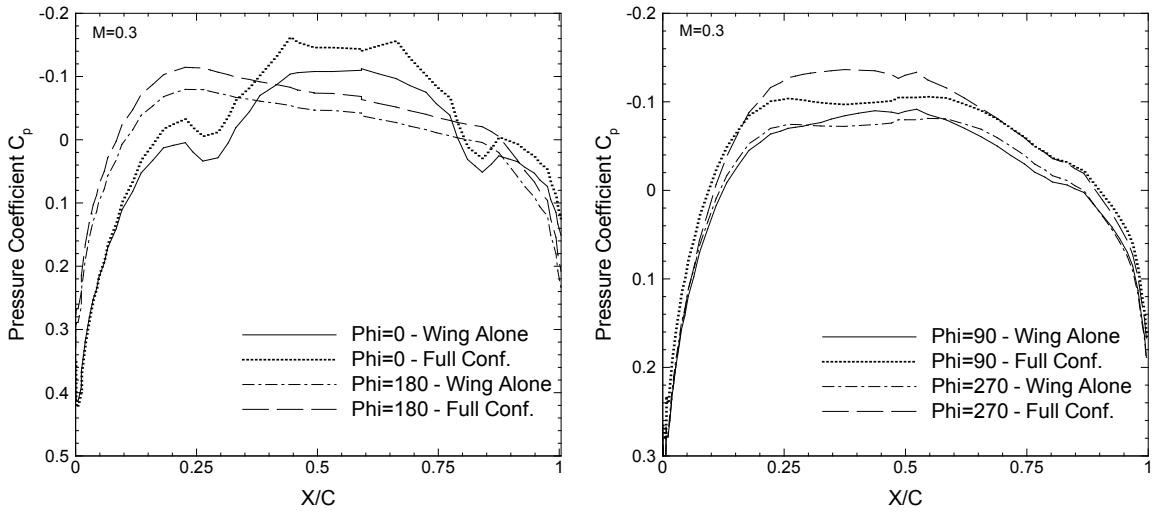

Figure 29: Pressure Distribution on the Fuel Tank in Captive Position, M=0.3.

There is a significant difference in side forces as observed in Figure 30. The negative side force on the store released from the full aircraft configuration shows a linear decrease as the store moves downwards. This result shows the predominant effect of including the fuselage to the modeling of a fuel tank separation problem. Also an increase in the lift and a decrease in the drag coefficient acting on the store is observed. A summary of the force and moment coefficients at the captive carriage state are given in Table 6.

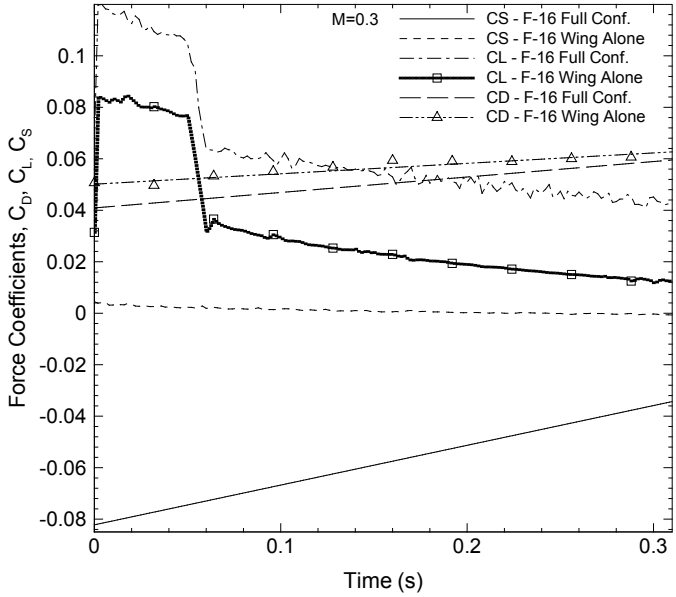

Figure 30: Time Histories of Force Coefficients, M=0.3.

3.4 Decoy Separation

The results obtained from 3FL-DYN are compared with those of transient 6DOF CFD analyses. 3FL-DYN's ability to capture the effects of the variation of center of gravity, Mach number and tail sizes is investigated. 3FL-DYN results are expected to be at least similar to the 6DOF CFD results in trend. The analysis conditions of transient CFD analyses are given in Table 7, while the overall analysis matrix is given in Table 8. Considering the cross matching of all the combinations of these analyses, in order not to overwhelm the reader, the results are given here with respect to a selected reference case. This case is the most probable configuration and flight condition used for the decoy design. The reference case has a Mach number of 0.6, CG position of 30% and a tail size of 100%. For the analysis matrix, apart from the values for the reference case, a center of gravity and a tail size value, which are going to reduce the static stability of the decoy, were selected.

Table 7: Analysis Conditions (CFD).

Boundary Conditions	Pressure-Farfield (Outer Boundary) Adiabatic "No-slip" wall (decoy)
Turbulence Model	Realizable k-epsilon
Air	Compressible Ideal-Gas
Solver Approach	Pressure-Based Coupled
Spatial Discretization	Second-Order, Green-Gauss Node Based
Total Grid Size	2798373
Motion	6DOF "Dynamic Mesh"
Time Step (ms)	0.05

Table 8: Analysis Matrix.

Mach Number	0.30	0.45	0.60
CG locations	10 %	30 %	
Tail Sizes	80 %	100 %	

The center of gravity of the decoy is measured from half of the length of the decoy (positive direction pointing towards the nose of the decoy) and given as the percentage fraction of the length. For instance, CG = 15% means that the center of gravity of the decoy is 0.15 L front of the half-length of the decoy. Tail size is varied by changing the chord of the tail and given as a percentage of the tail size of the reference case.

For the investigation of every variable, the pitch angle and the trajectories were compared with each other to observe the differences between the 3FL-DYN and 6DOF CFD analyses. In addition, to observe the trends more clearly, the results of 3FL-DYN for different variables and the results of the 6DOF CFD are plotted separately. (Figure 33 to Figure 36) Moreover, pressure and Mach number distributions around the decoy at different times are given in Figure 31 and Figure 32, where the decoy is colored with the gage pressure values. The horizontal and vertical distances covered by the decoy is scaled down to 2.5%, while the decoy itself is not scaled. According to the results:

- It is obvious that for the CG = 10% case the results are closer. This is due to the fact that initially as the decoy has a high AoA, CG = 30% case has a higher moment arm compared to the CG = 10% case for the pitching moment resulting in higher angular accelerations and oscillations. The same situation is valid also for the Tail = 100% case as well.
- It is clear that the magnitude of the oscillations of pitch angle are overestimated by the 3FL-DYN.
- As a trend, 3FL-DYN was able to capture the higher frequency of the oscillations for the forward center of gravity and higher Mach numbers. But as 6DOF CFD was able to dissipate more energy by damping mechanisms in the lateral directions, the magnitude of the oscillations decreases more rapidly as well as the frequency for 6DOF cases.
- Magnitude of oscillations in yaw direction is 5-7 times smaller than that of the pitch direction for all cases. CG = 10% and Tail Size = 80% cases have more oscillations in yaw direction due to lower correcting moments to the asymmetrical vortex shedding while the CG = 30% and Tail Size = 100% cases start rolling motion sooner as high AOA's are achieved faster. Similarly, higher the Mach number, higher the forces / moments and more effective the rolling motion is.
- The 3DOF method is more conservative for initial design purposes owing to the fact that the frequency and the magnitude of the oscillations are greater than that of the 6DOF CFD results.
- Decoy trajectories are captured very well by 3FL-DYN for all center of gravity positions.
- The comparisons of pitch angles, trajectories as well as the flowfield for the combinations of center of gravity, Mach number and tail size are proved to be coherent with the results explained above.
- It is clear that taking the size of the separation zones given in Figure 32, especially "a" and "b" time points, into account, the decoy is exposed to high angles of attack at every Mach number case. As time marches on due to the stabilization of the decoy, the separation zone sizes begin to decrease as the angle of attack values start to decrease.

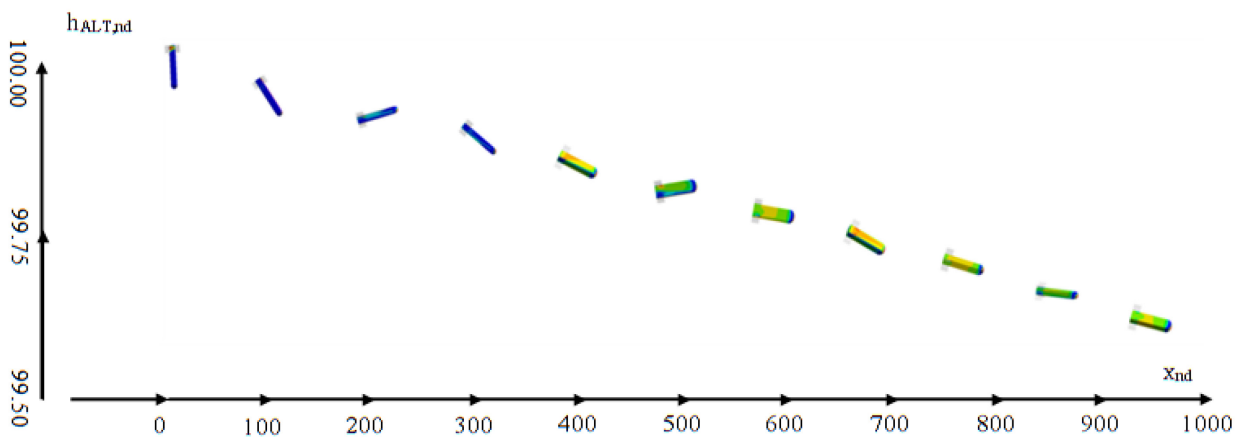

Figure 31: Sample Motion History of the decoy colored by gage pressure for M = 0.6, CG = 30%, Tail = 100% case.

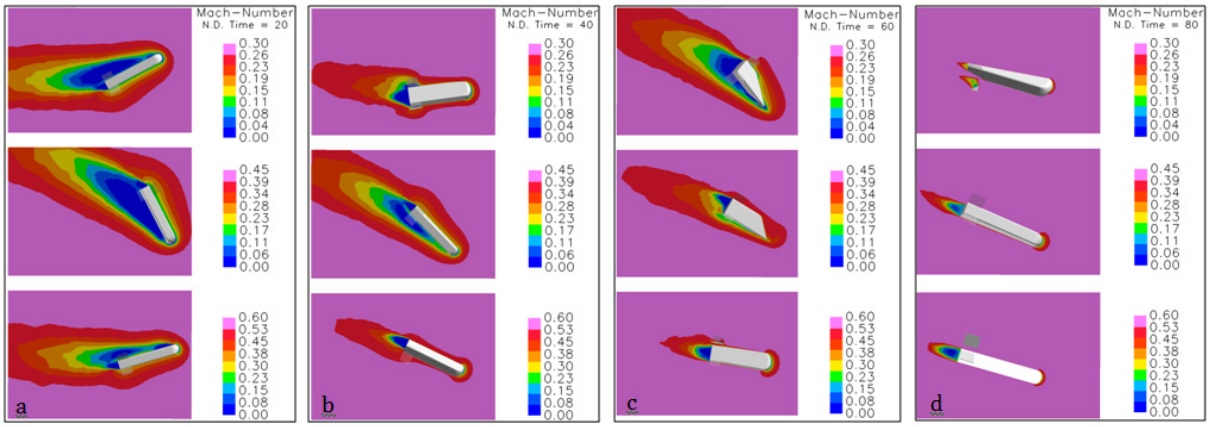

Figure 32: Mach number distribution around the decoy at four different time points (a,b,c,d) for M = 0.6 (bottom), M = 0.45 (middle) and M = 0.3 (top).

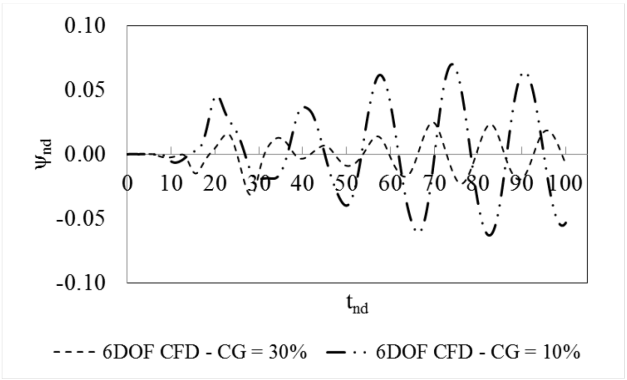

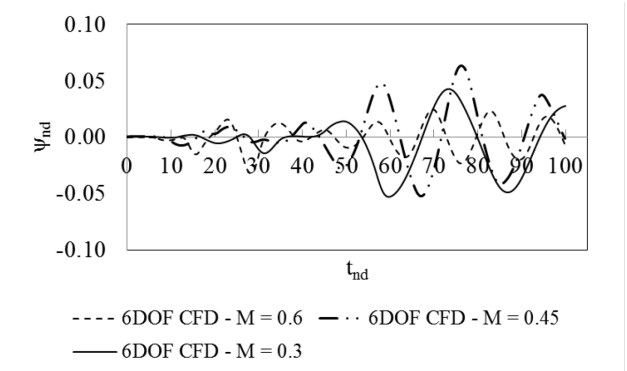

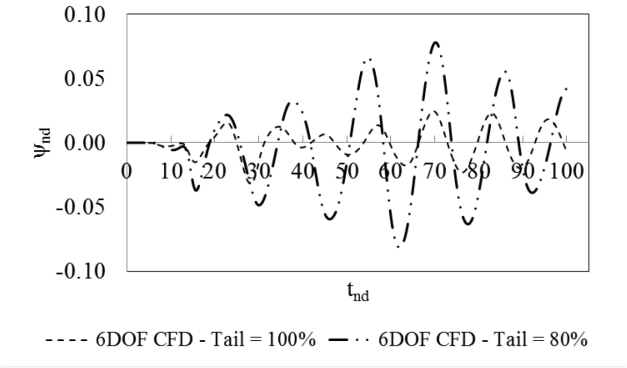

Figure 33: Time variation of yaw angle at obtained from 6DOF CFD for different Mach number, Tail Size and CG position combinations.

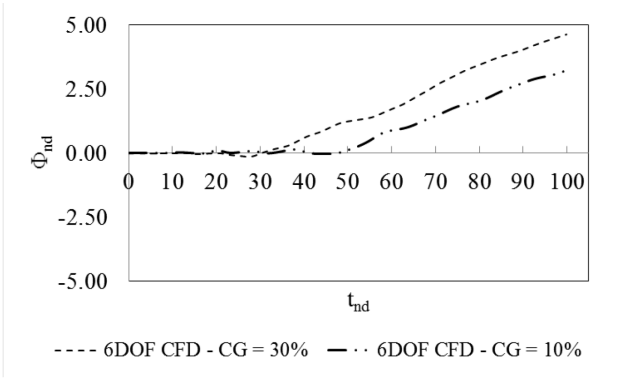

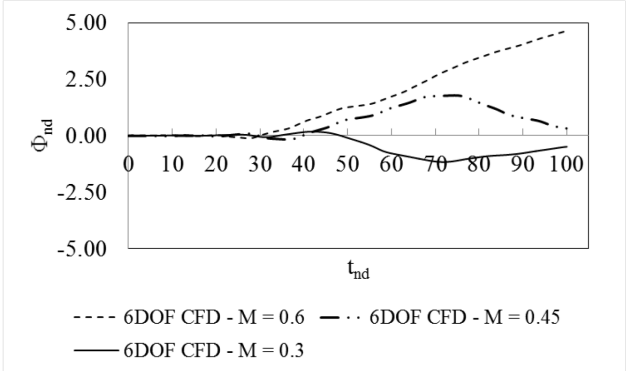

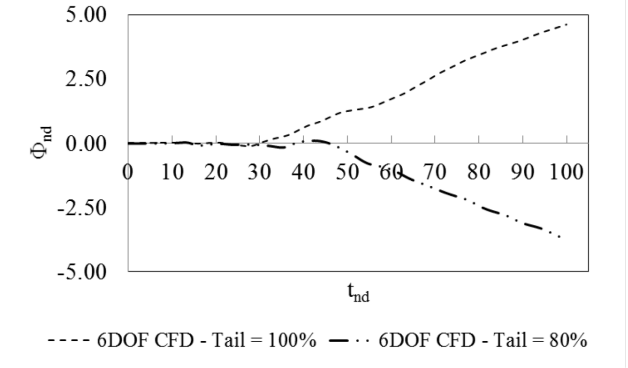

Figure 34: Time variation of roll angle at obtained from 6DOF CFD for different Mach number, Tail Size and CG position combinations.

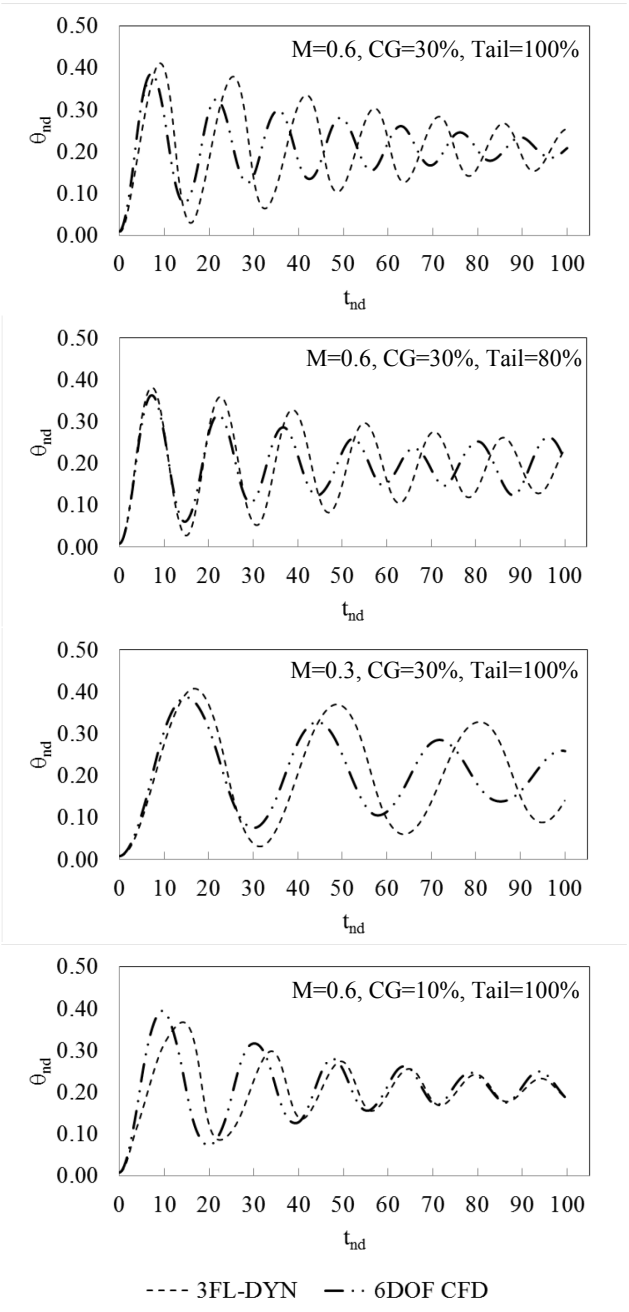

Figure 35: Comparisons of time variation of pitch angle obtained from 3FL-DYN and 6DOF CFD methods for different Mach number, Tail Size and CG position combinations.

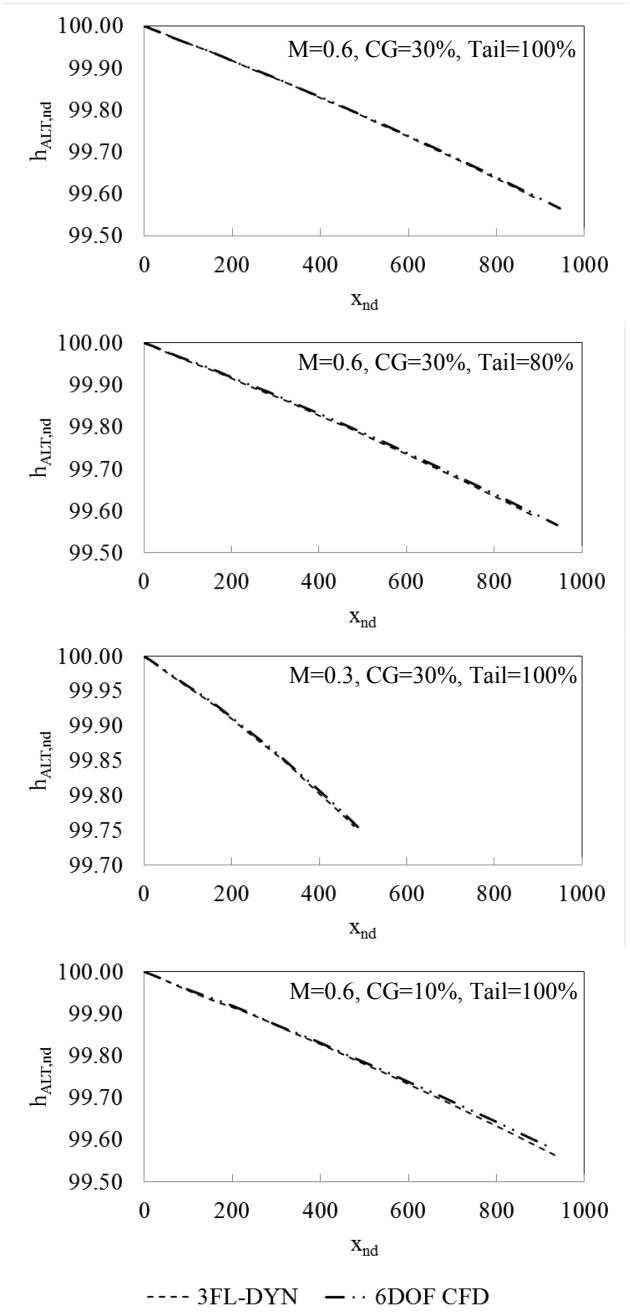

Figure 36: Comparisons of trajectories obtained from 3FL-DYN and 6DOF CFD methods for different Mach number, Tail Size and CG position combinations.

4.0 CONCLUSION

In this paper, three different studies are presented for the store separation CFD applications. Two of these studies are related to the CFD solution of Eglin Test Case, but with different grid generation and techniques used for the movement of the store inside the solution domain. Both solutions are obtained using Euler

method of solution. The first CFD code uses chimera technique of overset grids and the second CFD code uses grid deformation technique for the movement of the store. Both CFD codes are validated against the experimental data of Eglin test case at M=0.95. In the light of the present computational results, it is observed that the computational results are compatible with experimental data even though an inviscid solution is performed. To improve the computational solutions and avoid any discrepancy between the computational results and experimental data, viscous solution method should be obtained.

Separation of a fuel tank from an F-16 aircraft wing and full aircraft configurations are solved at Mach 0.3 using the unsteady panel code only. The increase in side force component of the store is observed after comparing the results obtained for the F-16 wing-pylon and full aircraft configurations using the USAERO panel code.

The three CFD methods can be used for the aerodynamic design and integration of a new store to an aircraft. Chimera overset grid and grid deformation method is well suited to the store separation problems. On the other hand, pre-processing and the solution time of the panel method are much less than the Euler method. Therefore, in order to have very fast results for large test matrices at low subsonic flow conditions, panel code should be preferred. On the other hand, Euler solutions must be used for shock dominated flows at transonic flow regimes.

The third study described a fast initial design methodology for a decoy and investigated the validity of the approach. For the decoy, a 3DOF motion assumption was discussed and the equations of motion were derived. The equations were numerically integrated by a code in a quasi-steady manner with the help of tabulated aerodynamic data. The aerodynamic coefficients in the tables were obtained from steady CFD calculations. An assessment of the methodology was made in terms of time step size selection for both 3FL-DYN and transient CFD calculations, grid independence, inclusion of the pitch damping term and the evaluation of 3DOF assumption. In these studies, time step and the grid size were selected such that the solution is independent from these numerical parameters. To validate the 3DOF initial design methodology, comparisons between the results obtained from 3FL-DYN and transient 6DOF CFD were carried out. The terms of comparisons were angular / translational velocities, accelerations, trajectories and angular positions. For comparing purposes, instead of expecting the results to be on top of each other, the ability to capture the effects of the variations of different variables such as Mach number, center of gravity and tail sizes was considered. But, as 3DOF method was found out to be more conservative, it was deemed sufficient for fast initial design purposes. The trajectories obtained from 3FL-DYN agreed very well with the 6DOF CFD results.

5.0 REFERENCES

[1] Demir, H.O. "*Computational Fluid Dynamics Analysis of Store Separation,*" MSc. Thesis, 2004, METU.

[2] Demir, G., *"Computational Fluid Dynamics Modeling of Store Separation Using Grid Method"* MSc. Thesis, In Progress, METU.

[3] Selimhocaoğlu, B.T., *"Aerodynamic and Three-Degree-of-Freedom Flight Mechanics Analysis of a Slender Body of Rectangular Cross Section"* MSc. Thesis, 2014, METU.

[4] Fox, J.H., "23. *Generic Wing, Pylon and Moving Finned Store,"* RTO-TR-26, Verification and Validation Data for Computational Unsteady Aerodynamics, October 2000.

[5] Lijewski, L.E., and Suhs, N.E., *"Time Accurate Computational Fluid Dynamics Approach to Transonic Store Separation Trajectory Prediction,"* Journal of Aircraft, Vol. 31. No. 4, pp. 886-891.

[6] Prewitt, N.C., Belk, D.M., and Maple, R.C., *"Multiple Body Trajectory Calculations Using the Beggar Code,"* Journal of Aircraft, Vol. 36, No. 5, 1999, pp. 802-808.

[7] Lee, S., and Park, M., Cho, K.W., Kwon., J.H., *"New Fully Automated Procedure for the Prediction of Store Trajectory,"* Journal of Aircraft, Vol. 37, No. 6, November-December 2000.

[8] Lijewski L.E., *"Transonic Euler Solutions on Mutually Interfering Finned Bodies"* AIAA Journal, Vol., 28, No. 6.

[9] Hall, L.H., Mitchell C.R., Parthasarathy, V., "*An Unsteady Simulation Technique for Missile Guidance and Control Applications,"* AIAA 97-0636, 35th Aerospace Sciences Meeting & Exhibit, January 6-10, 1997 / Reno, NV.

[10] Rock, S.G. and Habchi, S.D., Yeiser, C. and Oslon, M., Marquette, T., "*A computational Methodology for the Rapid Simulation of Jettisoned Aircraft Canopy Trajectories,"* AIAA 97-0169, 35th Aerospace Sciences Meeting & Exhibit, January 6-10, 1997 / Reno, NV.

[11] Hall L. "*Navier-Stokes/6-DOF Analysis of the JDAM store separation from the F/A-18C Aircraft,*" AIAA Paper 99-0121, January 1999.

[12] Chen, P.C., Liu, D.D., "*Store-Separation Analysis at Subsonic and Supersonic Speeds Using a High-Order Panel Method,*" AGARD 76th Fluid Dynamics Panel Meeting and Symposium on Aerodynamics of Store Integration and Separation, Ankara, Turkey, 24-28 April, 1995.

[13] *ANSYS FLUENT 16.2 User's Guide*, Fluent Inc., 2015.

[14] *ANSYS FLUENT 16.2 Theory Guide*, Fluent Inc., 2015.

[15] *Standard Atmosphere*. International Organization for Standardization, ISO 2533:1975, 1975.

[16] Canale, R.P., Chapra, S.C. *Numerical Methods for Engineers*. McGraw Hill, 6th ed, 2009.

[17] Versteeg, H., Malalasekra, W. *An Introduction to Computational Fluid Dynamics*. Pearson, 2nd ed., 2007.

[18] Wilcox, D.C. *Turbulence Modeling for CFD*. DCW Industries, Inc., 1994.

[19] *Altair HyperWorks Desktop 11*, Altair Engineering Inc., 2011.

[20] Siouris, G.M. *Missile Guidance and Control Systems*. Springer, 2004.

[21] Patel, M., Sowle, Z. et al. *Aerodynamic Control of a Small Projectile.* 44th AIAA Aerospace Sciences Meeting and Exhibit, AIAA 2006-667, 2006.

[22] Blakelock, J. *Automatic Control of Aircraft and Missiles*. John Wiley & Sons, s.230-231, 1991.